# nature chemistry

**Article** 

https://doi.org/10.1038/s41557-024-01689-5

# Electrochemical formation of bis(fluorosulfonyl)imide-derived solid-electrolyte interphase at Li-metal potential

Received: 25 April 2024

Accepted: 31 October 2024

Published online: 2 December 2024



Weilai Yu ®¹, Kuan-Yu Lin ®¹, David T. Boyle ®²³, Michael T. Tang ®¹⁴, Yi Cui ®³, Yuelang Chen ®¹², Zhiao Yu ®¹², Rong Xu ®³, Yangju Lin ®¹, Guangxia Feng ®³, Zhuojun Huang¹³, Lukas Michalek ®¹, Weiyu Li ®³⁵, Stephen J. Harris⁶, Jyh-Chiang Jiang⁷, Frank Abild-Pedersen ®⁴, Jian Qin ®¹, Yi Cui ®³⁵. & Zhenan Bao ®¹⊠

Lithium bis(fluorosulfonyl)imide-based liquid electrolytes are promising for realizing high coulombic efficiency and long cycle life in next-generation Li-metal batteries. However, the role of anions in the formation of the solid-electrolyte interphase remains unclear. Here we combine electrochemical analyses and X-ray photoelectron spectroscopy measurements, both with and without sample washing, together with computational simulations, to propose the reaction pathways of electrolyte decomposition and correlate the interphase component solubility with the efficacy of passivation. We discover that not all the products derived from interphase-forming reactions are incorporated into the resulting passivation layer, with a notable portion present in the liquid electrolyte. We also find that the high-performance electrolytes can afford a sufficiently passivating interphase with minimized electrolyte decomposition, by incorporating more anion-decomposition products. Overall, this work presents a systematic approach of coupling electrochemical and surface analyses to paint a comprehensive picture of solid-electrolyte interphase formation, while identifying the key attributes of high-performance electrolytes to guide future designs.

Improving the cycling stability of Li-metal anodes (LMAs) is a high priority goal for developing next-generation Li battery technology, with a potential to deliver an energy density of >500 Wh kg<sup>-1</sup> (ref. 1). However, large-scale commercialization of LMA technology is hindered by several long-standing challenges, in particular Li-dendrite formation and the uncontrolled reactivity at electrode/electrolyte interfaces<sup>2</sup>. The solid–electrolyte interphase (SEI) that forms either chemically or electrochemically at the surface of Li metal has been regarded as a key regulator of the interfacial stability of LMAs. Understanding the

fundamentals of SEI-formation reactions at Li-metal potential can guide the rational design of a robust SEI to minimize side reactions for improved battery performance.

Liquid electrolyte engineering has been proven to be an effective strategy for elevating the coulombic efficiency (CE) of LMAs to >99%, using a lithium bis(fluorosulfonyl)imide (LiFSI) salt $^{3-6}$ . The superior performance of LiFSI-based electrolytes has been ascribed to the beneficial role played by the anion-derived portion of the SEI, which is composed of inorganic species such as LiF $^7$ . Previous studies using

A full list of affiliations appears at the end of the paper. Me-mail: yicui@stanford.edu; zbao@stanford.edu

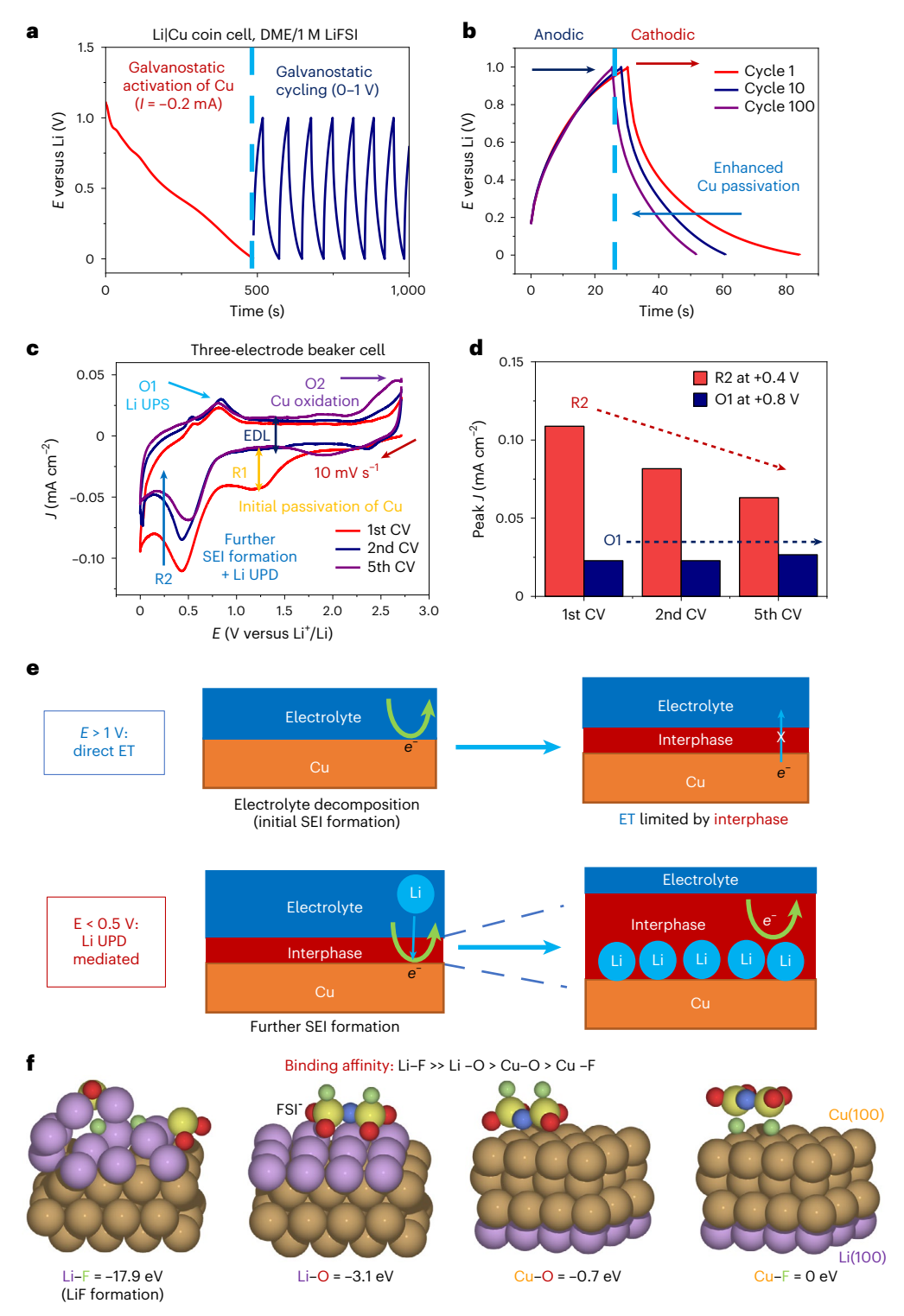


Fig. 1| Electrochemical reactivity of the baseline DME/1 M LiFSI electrolyte to form an interphase (SEI $_{cu}$ ) at the surface of a Cu electrode. a, A representative E-t profile for the initial galvanostatic activation of the Cu electrode (red) in a Li|Cu half cell, and its subsequent cycling between 0 and +1  $V_{Li}$  (blue) 100 times under constant current, |I| = 0.2 mA, in a baseline electrolyte composed of 1 M LiFSI dissolved in DME (DME/1 M LiFSI). b, Comparison of E-t curves obtained at the 1st, 10th and 100th cycles during the galvanostatic cycling in a. c, Comparison of the first five cycles for three-electrode CV of a mechanically polished Cu micro-electrode in DME/1 M LiFSI electrolyte; Li foils were used as both reference and counter electrodes; R and O represent reduction and oxidation waves,

respectively. Scan rate:  $10 \text{ mV s}^{-1}$ .  $\mathbf{d}$ , Comparison of  $|J_{peak}|$  for the reduction peaks (R2) at +0.4  $V_{Li}$  and the oxidation peaks (O1) at +0.8  $V_{Li}$  for the different CV cycles in  $\mathbf{c}$ .  $\mathbf{e}$ , Schematic illustration of a two-stage mechanism of  $SEl_{Cu}$  formation mediated by direct ET at high  $E_{Cu}$  (>+1  $V_{Li}$ ) and Li UPD at low  $E_{Cu}$  (<+0.5  $V_{Li}$ ), respectively.  $\mathbf{f}$ , DFT calculations of the binding affinity between the Cu(100) and Li(100) UPD layer and the different binding sites of FSI^ (O and F), revealing a trend of Li-F  $\gg$  Li-O > Cu-O > Cu-F. The same Cu(100)/Li(100)-UPD slab was used so that the differences in binding affinity could be compared strictly. The absolute energy of FSI^ adsorbed on the Cu(100) surface was used as the baseline (0 eV) to effectively compare the binding affinity in different atomic models.

cryogenic electron microscopy (cryo-EM) have directly visualized the SEI layer formed in these electrolytes to be structurally monolithic and compositionally heterogeneous, while minimized SEI swelling was found to correlate with a higher  $CE^{8-10}$ .

Although the presence of sulfur (S) in those SEIs signifies its origin from FSI<sup>-</sup> decomposition, a molecular-level understanding of the electrochemical reactions leading to SEI formation remains missing. A mechanistic study would require detailed investigation of charge-transfer processes at the electrochemical interface. For LiFSI-based electrolytes, a quantitative correlation remains to be established between the interfacial reactivity of anion-decomposition processes, the passivation efficiency of anion-derived SEI layers, as well as the resulting cycling efficiency of Li-metal batteries. Such a detailed understanding will not only uncover the origin of the coulombic inefficiency that impacts long-term battery cyclability, but also inform design principles for liquid electrolytes to enable more effective SEI passivation 11-13. Furthermore, revealing the dissolution of soluble products derived from SEI-forming reactions is equally important for comprehensively understanding the passivation behaviour of Li<sup>0</sup> metal<sup>14,15</sup>.

In this Article, we combine electrochemical analyses with X-ray photoelectron spectroscopy (XPS) to elucidate the electrolytedecomposition pathways as well as the formation mechanism of FSI<sup>-</sup>derived SEI in ether-based electrolytes, which are further substantiated by computational simulations. A planar Cu electrode was used, because this is a well-defined platform with which to probe the electrochemical processes of SEI formation as a function of driving force, as the applied potential on a Cu current collector ( $E_{Cu}$ ) gradually approaches the Li<sup>0</sup>-metal potential (0 V<sub>1i</sub>). Sample washing is a common practice for XPS analysis in the battery field16, but we instead designed a non-washing protocol to capture reaction products that would otherwise have been lost to resolve the basic steps of FSI breakdown, as well as revealing the partial dissolution of SEI-reaction products<sup>17</sup>. By comparing the XPS data obtained with and without sample washing, we determined the varied contributions of different inorganic species from FSI<sup>-</sup> breakdown to form a passivating SEI over the Cu surface, according to their solubility trends. This work bridges the critical knowledge gap regarding SEI formation processes for liquid electrolytes consisting of ether solvent and LiFSI, and this analytical approach can be broadly extended to rationalize the reactivity of other promising electrolytes.

# **Results and discussion**

# Electrochemistry of SEI-forming reactions at a Cu surface

We first probed SEI formation on the Cu current collector surface (SEI<sub>CII</sub>) in Li|Cu coin cells with a baseline liquid electrolyte consisting of 1.0 M LiFSI salt dissolved in 1,2-dimethoxyethane (DME) solvent (DME/1 M LiFSI)<sup>5,6,18</sup>. Chronopotentiometry (CP) at a constant current of |I| = 0.2 mA was applied to cycle the Li|Cu cells between 0 and +1  $V_{Li}$ , without plating any bulk Li metal (Fig. 1a). A comparison of potential-time (E-t) profiles during galvanostatic cycling showed that the initial drop in  $E_{Cu}$  to 0  $V_{Li}$  took much longer than in all subsequent cycles (Fig. 1b). In later cycles, the duration of cathodic scans gradually decreased with the cycle number, although the shape of the anodic scans remained similar. An analysis of integral charge (Q) during this CP cycling showed that additional charges involved in the cathodic scans decreased with increasing cycling, whereas the Q-t profile in the 100th cycle became nearly symmetric (Supplementary Fig. 1), signalling reversible processes such as electric double layer (EDL) charging. In this regard, the extra cathodic charge involved in the earlier CP cycles is attributed to irreversible SEI<sub>Cu</sub> formation.

Three-electrode cyclic voltammetry (CV) was then used to resolve the  $\emph{E}$ -dependent reactivity at the Cu/electrolyte interface (Fig. 1c). The first CV scan exhibits a notable reduction wave (**R1**) from +2 to +1  $V_{\rm Li}$  that disappears in later CV cycles, suggesting the irreversible SEI<sub>Cu</sub>

formation. The rapid increase in current density (1) with an onset of  $E_{CII} \approx +1.75 \, V_{Li}$  shows an accelerated electrochemical reaction with increasing driving force at the pristine Cu-electrolyte interface<sup>19</sup>. The flat features from the second to the fifth CV cycles in the same E region are characteristic of EDL charging. Correlated reduction (R2) and oxidation (O1) waves can be observed at  $E_{CII} \sim +0.4$  and +0.8  $V_{II}$ , respectively, with minor oxidation peaks at ~+0.6 V<sub>II</sub>. Previous studies attributed these redox waves to the under-potential deposition (UPD) and stripping (UPS) of Li that presumably occurs beneath the initially formed SEI<sub>CII</sub> (ref. 20). The two distinct oxidation peaks have been attributed to different crystal facets of a polished Cu surface<sup>20,21,22</sup>. Evident oxidation waves (O2) in Fig. 1c gradually emerge at high  $E_{Cu} > +2 V_{Li}$  during CV cycling, and these were assigned to Cu<sup>0</sup> oxidation, possibly due to the newly formed Cu<sup>0</sup>/Li<sub>2</sub>O interface<sup>23,24</sup>. However, a direct comparison of absolute current densities  $(|J_{\text{peak}}|)$  shows that the  $|J_{\text{peak}}|$  values of the R2 peaks are much larger than those of the O1 peaks (Fig. 1d). As CV cycling progresses, the  $|J_{peak}|$  of the R2 peaks gradually decreases, whereas the  $|J_{\text{peak}}|$  of the O1 peaks remains nearly unchanged. These results suggest the reversible character of Li UPD/UPS (O1) occurring at the Cu surface, while highlighting the parasitic irreversible contributions embedded in the R2 peaks that account for further SEI<sub>Cu</sub> formation following R1. Addi $tional\,CV\,data\,measured\,in\,Li|Cu\,coin\,cells\,reproduced\,similar\,features$ in the initial and subsequent SEI<sub>Cu</sub> formation (Supplementary Fig. 2).

Based on these results, we propose that  $SEI_{cu}$  formation occurs via a two-stage mechanism that gives rise to the E-dependence (Fig. 1e). At higher  $E_{Cu} > +1$   $V_{Li}$ , the  $SEI_{Cu}$  initially forms via direct electron transfer (ET) at the Cu/electrolyte interface, causing decomposition of the solvent and salt species (DME/LiFSI). The absence of an R1 peak in the later CV cycles suggests that a sufficiently thick  $SEI_{Cu}$  inhibits effective  $ET^{25,26}$ . At lower  $E_{Cu} < +0.5$   $V_{Li}$ , further  $SEI_{Cu}$  formation can be mediated by the Li UPD process that probably occurs at the Cu/ $SEI_{Cu}$  interface, leading to superimposed reductive waves (R2) $^{27,28}$ . Within the confined space of  $SEI_{Cu}$ , effective ion transport from the outer electrolyte towards the inner Cu surface can be facilitated by SEI swelling $^{10}$ . Under cathodic conditions, the reduction of  $Li^+$  cations to form Li UPD layers can simultaneously trigger further decomposition of  $FSI^-$  anions to enhance  $SEI_{Cu}$  formation.

As Li UPD can change the surface reactivity of the Cu electrode by depositing monolayers of Li atoms, such an E-dependent electrolyte decomposition may be an inner-sphere ET process involving active molecular binding to a specific metal surface  $^{29}$ . We applied density functional theory (DFT) calculations to compare the binding affinity of an FSI $^-$  anion on a representative Cu(100) surface versus a Li(100) UPD layer (Fig. 1f). Both the negative adsorption energies of a single Li atom and a Li(100) slab on the Cu(100) surface verify that the formation of Li UPD layers is thermodynamically favourable (Supplementary Table 2). Furthermore, the calculation results consistently show a considerably higher affinity of FSI $^-$  bound to a Li(100) surface than a Cu(100) surface, which explains the higher electrochemical reactivity during Li UPD. Notably, the Li(100) and Cu(100) surfaces show different binding affinities to the O and F sites of FSI $^-$ , whereas the strong Li–F interaction readily breaks down FSI $^-$  into LiF.

# XPS of non-washed versus washed Cu electrodes

To probe the chemical origin of electrolyte reactivity, we carried out XPS measurements with a designed non-washing protocol to preserve all solid products derived from  $SEl_{Cu}$ -forming reactions, especially those partially soluble in liquid. Following the rationale in Supplementary Note 1, we systematically compared XPS measurements for non-washed and washed Cu electrodes undergoing the same galvanostatic cycling (CP-Cu). Our previous XPS benchmark of the LiFSI salt allows for reliable identification of key reaction products from  $SEl_{Cu}$  reactions  $I^T$ .

First, a comparison of the C 1s sputtering profiles in Fig. 2a–c reveals contrasting spectra for the non-washed and washed CP-Cu samples, confirming that the non-washing protocol produces a separate

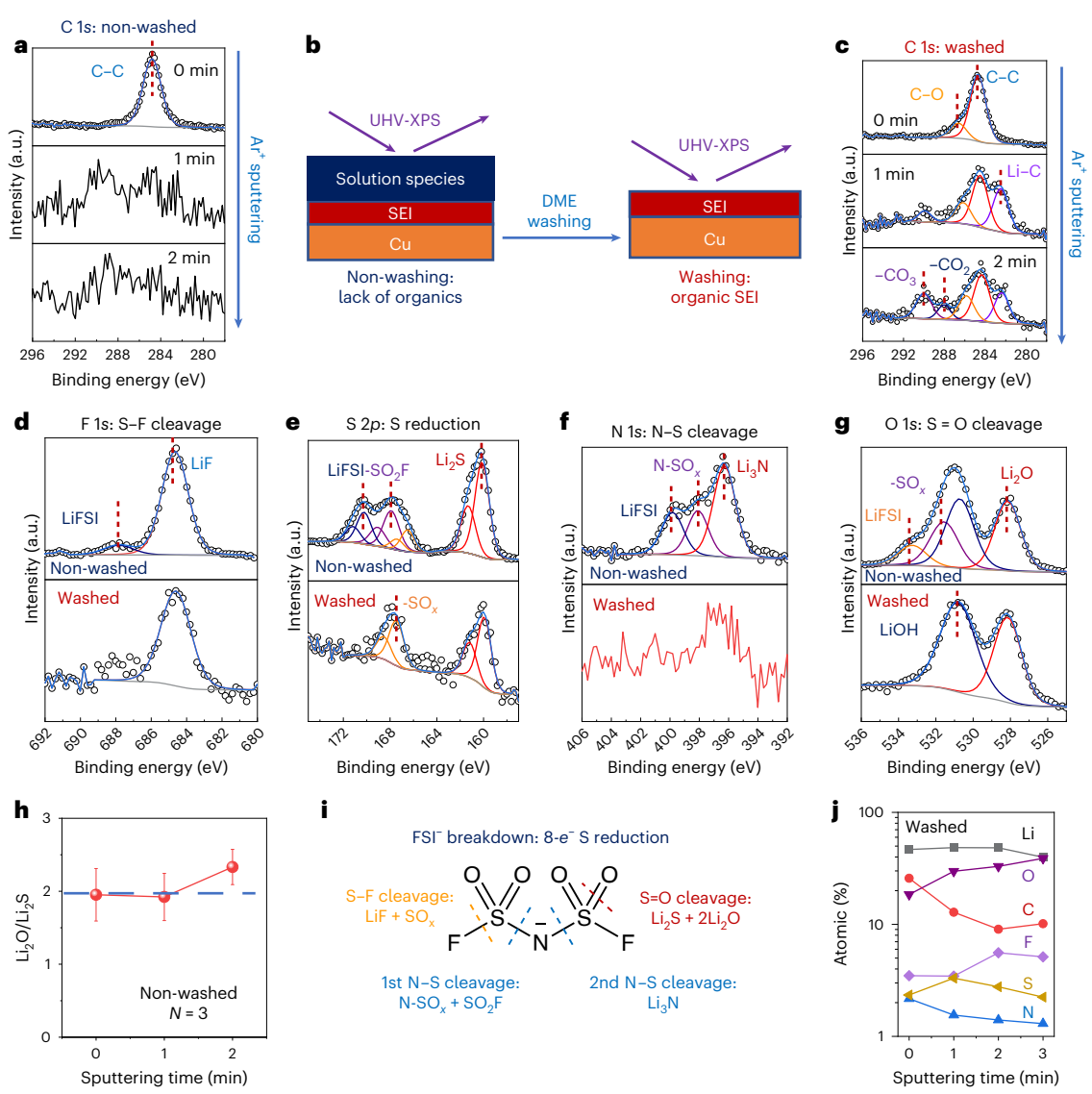


**Fig. 2** | **Identification of key reaction products dictating the elementary steps of FSI**<sup>-</sup>-**derived SEI chemistry.**  $\mathbf{a}$ - $\mathbf{c}$ , Comparison of high-resolution C 1 $\mathbf{s}$  sputtering profiles for non-washed ( $\mathbf{a}$ ) and washed ( $\mathbf{c}$ ) Cu electrodes galvanostatically cycled between 0 and +1  $V_{L1}$  100 times at |I| = 0.2 mA (CP-Cu). The same low-power (1 kV) Ar' sputtering setting was used to enable systematic comparison.  $\mathbf{d}$ - $\mathbf{g}$ , Comparison of high-resolution XPS surface spectra in F1 $\mathbf{s}$  ( $\mathbf{d}$ ), S 2p ( $\mathbf{e}$ ), N1 $\mathbf{s}$  ( $\mathbf{f}$ ) and O1 $\mathbf{s}$  ( $\mathbf{g}$ ) regions for the same non-washed (upper) and

washed (lower) CP-Cu samples.  $\mathbf{h}$ , Averaged Li<sub>2</sub>O/Li<sub>2</sub>S atomic ratios of replicate non-washed CP-Cu samples with increasing sputtering time. Data are presented as mean values  $\pm$  s.d., and three independent samples were measured (N=3).  $\mathbf{i}$ , Schematic illustration of the elementary steps of FSI breakdown into various inorganic species based on observations of the CP-Cu samples.  $\mathbf{j}$ , Atomic percentage of the representative washed CP-Cu sample with increasing sputtering time.

solution-precipitate (SP) layer. Although both sample surfaces were dominated by adventitious carbon, the absence of post-sputtering C 1s signals for the non-washed sample implies a lack of organic species within the SP layer. By contrast, the post-sputtering profiles of the washed CP-Cu sample reveal organic species enriched with C–C/H (284.8 eV), Li $^+$ C $^-$ (-282.5 eV), C–O (-286.5 eV), O–C–O (-288.5 eV) and -CO $_3$ (-290 eV), which are attributed to decomposition of the DME solvent $^{^{30}}$ .

To discount salt decomposition by Ar $^+$  sputtering, we further compared the XPS surface spectra of other inorganic elements in both non-washed and washed CP-Cu samples. For a non-washed sample, the substantial LiF (-90 at%) peak at binding energy (BE) = 684.8 eV relative to the LiFSI peak (688.0 eV) suggests pronounced S-F bond cleavage due to electrochemical reactions (Fig. 2d) $^{31}$ . Besides the LiFSI peak at BE = 170.3 eV in the S 2p spectra $^{17}$ , three distinct doublets at lower BEs of -168, 166.5 and 160 eV are assigned to the -SO $_2$ F fragment, oxidized sulfur (SO $_2$ ) and Li $_2$ S, respectively (Fig. 2e) $^{32,33}$ . The

SO<sub>x</sub> formation corresponds to the S-F cleavage of FSI<sup>-</sup>. The presence of Li<sub>2</sub>S shows a reduction in the S oxidation state from +6 (LiFSI) to -2 (Li<sub>2</sub>S), leading to a dramatic decrease in BE by >10 eV. Deconvolution of the N1s spectrum in Fig. 2f reveals three distinct peaks with comparable intensities at ~399.8, 398 and 396.2 eV, respectively. The highest- and lowest-BE peaks are assigned to LiFSI and Li<sub>3</sub>N, respectively, following the number of N-S bonds<sup>17,34</sup>. Therefore, the emergence of the middle peak at BE = 398 eV can be attributed to a N-SO<sub>x</sub> intermediate with a single N-S bond. The O 1s spectrum also shows peaks assigned to LiFSI (533.3 eV), SO<sub>x</sub> (531.6 eV), LiOH (530.7 eV) and Li<sub>2</sub>O (528.2 eV), respectively (Fig. 2g)<sup>34</sup>. Moreover, the Li<sub>2</sub>O/Li<sub>2</sub>S ratios were consistently determined to be ~2 (Fig. 2h) throughout Ar<sup>+</sup> sputtering, matching well the chemical stoichiometry of LiFSI. Moreover, the XPS sputtering profiles reveal a tendency for the FSI-decomposition products (Li<sub>2</sub>S, Li<sub>3</sub>N and Li<sub>2</sub>O) to accumulate on top of the SP layer (Supplementary Fig. 3). Additional Raman analysis of the non-washed CP-Cu sample shows the disappearance of several

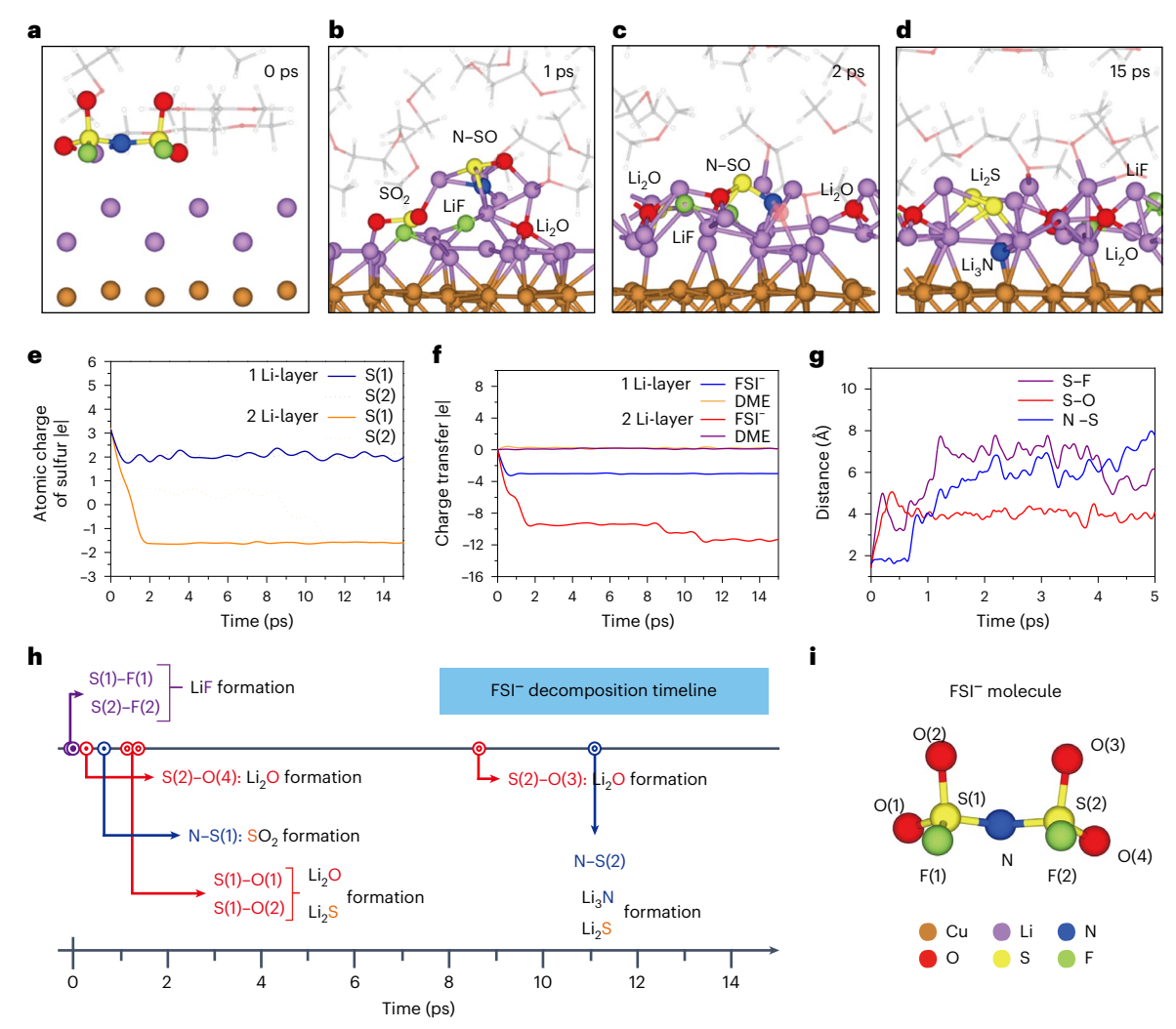


**Fig. 3** | **AIMD simulation of FSI**<sup>-</sup> **decomposition. a-d**, Representative snapshots from MD simulations depicting FSI <sup>-</sup> decomposition at 0 (**a**), 1 (**b**), 2 (**c**) and 15 ps (**d**) on a bilayer Li(100) surface on top of a Cu(100) surface. **e-g**, Temporal evolution of the charge-transfer processes from Li<sup>0</sup> metal (single- and bilayer) to FSI <sup>-</sup> and DME (**e**), changes in the atomic charge of two different S atoms (**f**)

and changes in the bond distance of S–F, S–O and N–S bonds  $(\mathbf{g})$  during MD simulations.  $\mathbf{h}$ , Timeline of FSI $^-$  decomposition on the Li $^0$  bilayer surface model.  $\mathbf{i}$ , Illustration and atom labelling of the FSI $^-$  molecule. Orange, copper; purple, lithium; blue, nitrogen; red, oxygen; yellow, sulfur; green, fluorine.

signature vibrational modes of LiFSI, confirming FSI<sup>-</sup> decomposition (Supplementary Fig. 4)<sup>35</sup>.

Collectively, these data reveal three elementary steps of electrochemical FSI<sup>-</sup> breakdown at Li-metal potential (Fig. 2i), without actively plating Li metal: (1) S–F cleavage to form LiF and SO<sub>x</sub>, (2) stepwise N–S cleavage to produce the N–SO<sub>x</sub> intermediate and Li<sub>3</sub>N and (3) S=O bond cleavage to form stoichiometric amounts of Li<sub>2</sub>O/Li<sub>2</sub>S-2. The S atoms of FSI<sup>-</sup> act as the reductive centre at the Cu/electrolyte interface to trigger these bond-cleavage events, following an  $8e^-$  transfer process.

After deconvoluting the XPS spectra of the non-washed CP-Cu sample, we compared the XPS data for non-washed and washed CP-Cu samples to uncover the effective passivating ingredients of  $SEl_{Cu}$ . The absence of LiFSI peaks in Fig. 2d-g confirms successful removal of residual electrolyte to expose the underlying  $SEl_{Cu}$  layer. The  $SEl_{Cu}$  layer mainly consists of LiF,  $Li_2S$ ,  $-SO_{xr}$  LiOH/ $Li_2O_2$  and  $Li_2O$ . A comparison of atomic percentages shows a compositional trend of Li>O>C>F>S>N (Fig. 2j). LiOH/ $Li_2O$  and organic SEI species are the major components of  $SEI_{Cu}$ , with the other  $FSI^-$ -derived species (F/S/N) only constituting <5 at% (ref. 36). The XPS sputtering profiles in Supplementary Fig. 5 show a homogeneous composition distribution throughout the

 ${\rm SEI_{Cu}}$  layer, with the exception that  ${\rm SO}_x$  mainly appears at the surface. By constraining the full-width at half-maximum (FWHM), the Li 1s surface spectra can be deconvoluted into four different peaks. The peaks from 55.4, 54.5 and 53.5 eV are assigned to LiF, LiOH and Li<sub>2</sub>O, respectively<sup>34</sup>. Interestingly, the distinct Li1s peak with the lowest BE of ~52.1 eV may be assigned to either LiH from solvent/water reduction or metallic Li<sup>0</sup> formed by Li-UPD (Supplementary Fig. 6)<sup>31,34,37,38</sup>. Notably, this low-BE peak gradually diminished upon Ar<sup>+</sup> sputtering, signalling its high sensitivity<sup>37</sup>.

XPS measurements of replicate samples of non-washed and washed CP-Cu electrodes reproduced similar XPS spectra, demonstrating high consistency in both the FSI $^-$  decomposition and DME washing (Supplementary Figs. 7 and 8). An additional XPS dataset collected for a non-washed Cu electrode potentiostatically held at +1  $V_{\rm Li}$  showed similar products (LiF, Li $_2$ S and Li $_3$ N), indicating complete decomposition of FSI $^-$  at a potential much more positive than the Li-metal potential (Supplementary Fig. 9).

A systematic comparison between the XPS datasets obtained from the non-washed and washed Cu samples can reveal a relative solubility trend of different SEI ingredients. The distinct distributions of different species in the SP and  $SEI_{Cu}$  layers suggest that not

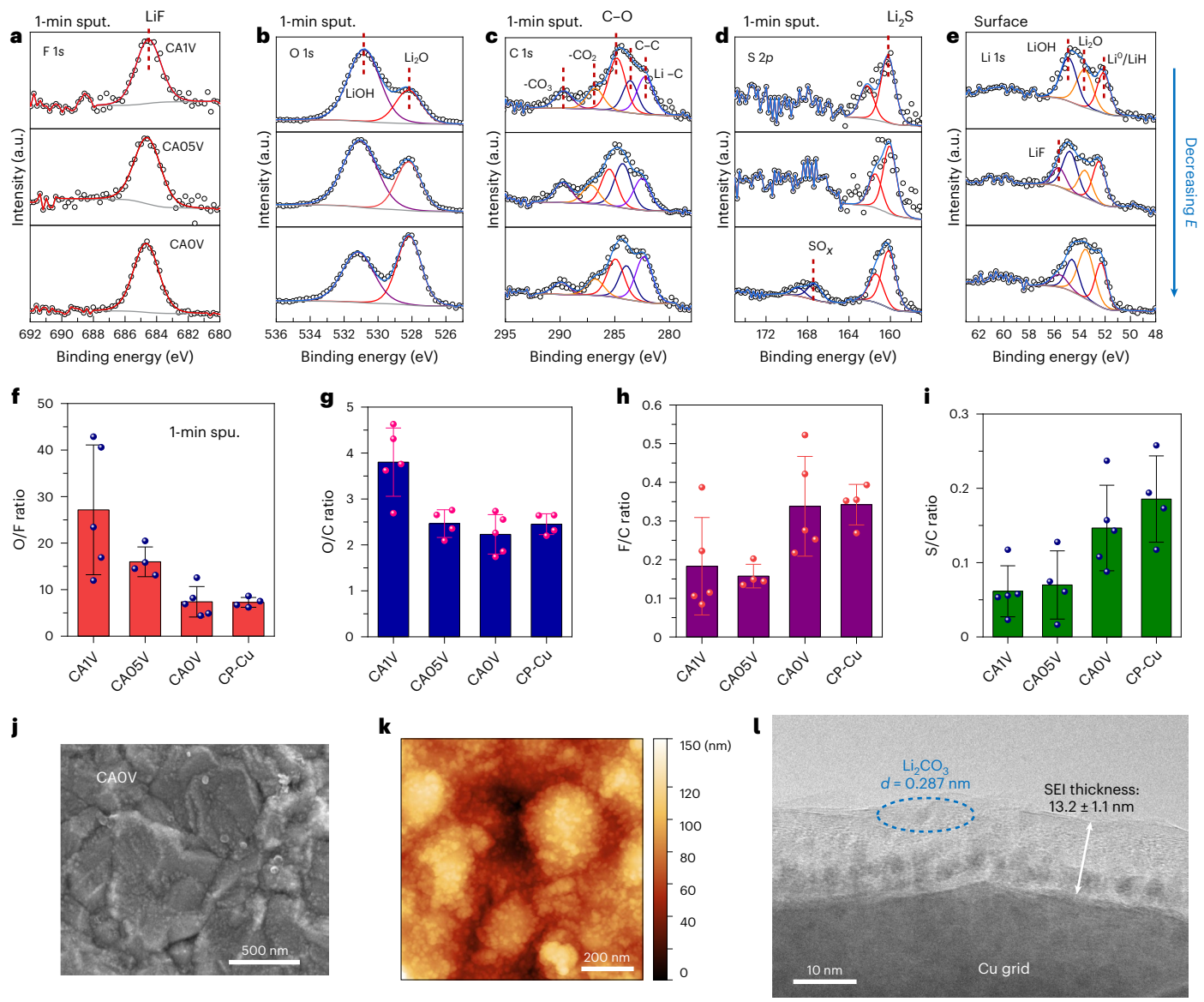


**Fig. 4** | *E*-dependent evolution of  $SEl_{Cu}$  composition. a-e, Comparison of high-resolution XPS spectra of F1s (a), O1s (b), C1s (c) and S2p (d) regions after 1-min Ar<sup>+</sup> sputtering, as well as Li1s surface spectra (e) measured for washed CA-Cu electrodes formed at varied E (from top to bottom, +1, +0.5 and 0  $V_{Li}$ ) for 3 h. Sputtering allows the effective removal of surface residuals such as adventitious carbon and oxidized sulfur (SO,), for comparison of the bulk

chemical composition of  $SEI_{Cu}$ .  $\mathbf{f}$ - $\mathbf{i}$ , Statistical analyses of different atomic ratios based on XPS data collected after 1 min of sputtering: O/F ( $\mathbf{f}$ ), O/C ( $\mathbf{g}$ ), F/C ( $\mathbf{h}$ ) and S/C ( $\mathbf{i}$ ). Data are presented as mean values  $\pm$  s.d. Sample size N is defined as the number of independent regions measured by XPS across each sample: N = 5 for CAIV and CAOV; N = 4 for CAO5V and CP-Cu. $\mathbf{j}$ - $\mathbf{l}$ , Morphological characterization of SEI<sub>Cu</sub> formed by CA at O V<sub>1</sub>, by SEM ( $\mathbf{j}$ ), AFM ( $\mathbf{k}$ ), cryo-EM ( $\mathbf{l}$ ).

all the products derived from  $SEI_{Cu}$  reactions contribute to passivation of the Cu surface, whereas a substantial portion dissolved into the solution. The substantial  $SO_x$ ,  $-SO_2F$  and N-containing species in the SP layer contrast with their negligible presence in the  $SEI_{Cu}$  layer, reflecting their high solubilities. The higher LiF content than Li<sub>2</sub>S in  $SEI_{Cu}$  suggests a lower solubility of LiF, considering the LiFSI stoichiometry (F/S = 1). A solubility trend can be estimated based on their relative abundance in  $SEI_{Cu}$ :  $Li_3N/N-SO_x/-SO_2F > SO_x > Li_2S > LiF > Li_2O/LiOH$ .

We also conducted ab initio molecular dynamics (AIMD) simulations to investigate the reaction details of FSI decomposition at picosecond time resolution. Two computational models with one and two Li(100) overlayers on a Cu(100) surface were constructed, respectively, to compare their different reactivities with Li $^+$ -FSI ion pairs (1 M) surrounded by DME solvent (Supplementary Fig. 10). Consistent with previous XPS analyses, snapshots of AIMD simulations of the bilayer

Li model in Fig. 3a-d clearly reveal complete breakdown of FSI into LiF, Li<sub>2</sub>O, Li<sub>2</sub>S and Li<sub>3</sub>N species, while the DME solvent remained relatively stable<sup>39,40</sup>. By contrast, the single-layer Li model exhibited much lower reactivity and only caused the S-F bond cleavage of FSI to form LiF (Supplementary Fig. 11). Correspondingly, Fig. 3e shows a more pronounced ET activity from the bilayer Li<sup>0</sup> surface to FSI<sup>-</sup> when compared to the single-layer model. This results in a concurrent increase and decrease of density of states (DOS) in the valence band (VB) and conduction band (CB) of the FSI- anion after 15 ps, respectively (Supplementary Fig. 12). The atomic-charge analyses in Fig. 3f show that the bilayer Li model causes its atomic charge to decrease to ~-2|e| via Li<sub>2</sub>S formation, confirming S atoms as the ET centre. Temporal evolution of the different bond distances of FSI reveal the order of the initial bond-cleavage processes (1 ps): S-F(both) > S-O > N-S, forming LiF, Li<sub>2</sub>O, SO<sub>2</sub> and NSO fragments (Fig. 3g,h). At 2 ps, the S-O bond in SO<sub>2</sub> completely breaks and forms Li<sub>2</sub>S and Li<sub>2</sub>O. At 11 ps, a complete

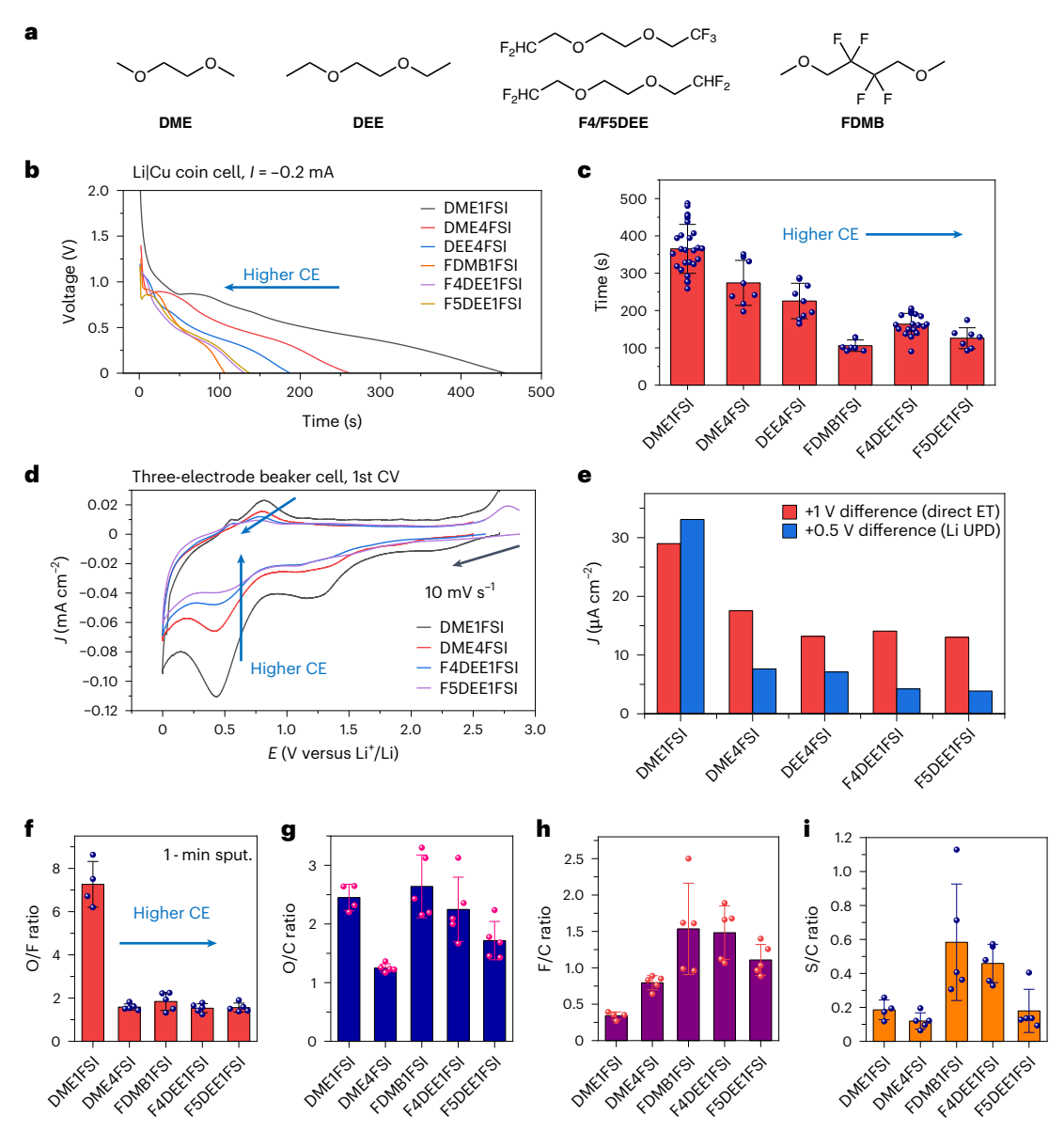


**Fig. 5** | **Comparison of interfacial reactivity and passivation for high-performance electrolytes. a**, Comparison of the molecular structures of different organic solvents enabling a high CE of >99% for LMAs. **b**, Comparison of representative E-t profiles during the galvanostatic testing of Li|Cu cells at I=-0.2 mA for different liquid electrolytes, showing that higher-CE electrolyte tends to exhibit shorter  $t_{\rm OV}$ . **c**, Statistical analysis of the  $t_{\rm OV}$  values in **b**. Data are presented as mean values  $\pm$  s.d. Sample size N is defined as the number of independent replicate cells tested, as shown in Supplementary Table 3. **d**, Comparison of the first CV of a Cu micro-electrode in contact with different

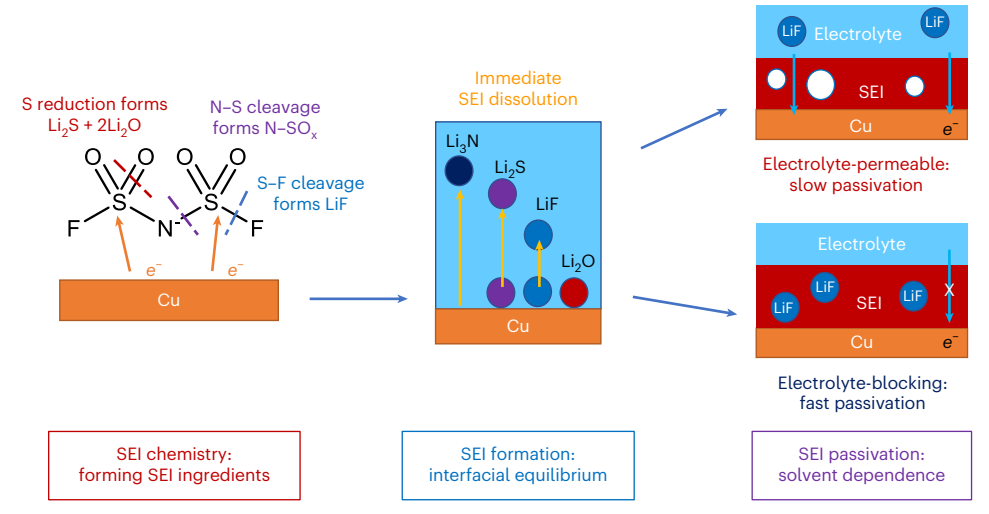
electrolytes in a three-electrode beaker cell, showing lower interfacial Cu reactivity for a high-CE electrolyte. **e**, Comparison of the differences in current densities ( $\Delta J$ ) at +1.0 V<sub>Li</sub> and +0.5 V<sub>Li</sub>. **f-i**, Comparison of different atomic ratios for the SEI<sub>Cu</sub> layers of CP-Cu samples formed in different electrolytes: O/F (**f**), O/C (**g**), F/C (**h**) and S/C (**i**). The XPS data collected after 1 min of sputtering were used for statistical comparison. Data are presented as mean values  $\pm$  s.d. Sample size *N* is defined as the number of independent regions measured by XPS across each sample: N = 4 for DME1FSI; N = 5 for the others.

FSI $^{\circ}$  breakdown to Li $_3$ N and Li $_2$ S is observed following the second step of N-S bond cleavage.

Next we revealed the  $SEI_{Cu}$  evolution by comparing the XPS data of washed Cu samples undergoing chronoampermetry at varied constant E (CA-Cu) (Supplementary Fig. 13). For a systematic comparison, we selected the XPS data collected after 1 min of  $Ar^+$  sputtering to exclude any surface adventitious species. The XPS spectra in Fig. 4a–d show nearly the same components of  $SEI_{Cu}$  formed under varied  $E_{Cu}$ , including LiF, LiOH, Li<sub>2</sub>O, C-species (Li–C, C–C, C–O, -CO<sub>2</sub> and -CO<sub>3</sub>) and Li<sub>2</sub>S. Possible C-containing SEI species include Li<sub>2</sub>CO<sub>3</sub>, LiOCH<sub>3</sub> and Li<sub>2</sub>C<sub>2</sub>, and so on (Supplementary Scheme 2)<sup>41,42</sup>. The Li 1s surface spectra presented in Fig. 4e consistently show the low-BE Li 1s peak at

 ${ extstyle -52}$  eV, besides Li ${ extstyle 2}$ O, LiOH and LiF. Notably, the relative content of Li ${ extstyle 2}$ O to LiOH gradually increased at more negative E (Fig. 4b). We also note that the broad O1s peaks centred at  ${ extstyle -531.0}$  eV exhibit a larger FWHM of  ${ extstyle >}2.2$  eV than those of Li ${ extstyle 2}$ O peaks ( ${ extstyle -1.6}$  eV), possibly due to convoluting contributions from additional species such as surface hydroxyl groups ( ${ extstyle -}$ OH) or lithium peroxide ( ${ extstyle Li}_2{ extstyle 0}_2$ ) $^{43,44}$ . All washed Cu samples exhibited weak N 1s signals, again reflecting the soluble nature of N-containing species (Supplementary Fig. 14).

Despite the lack of spectroscopic distinctions, statistical analysis of the different atomic ratios shows the compositional evolution according to the applied  $E_{\text{Cu}}$  (Fig. 4f–i). Changing  $E_{\text{Cu}}$  from +1 to 0  $V_{\text{Li}}$  caused the SEI<sub>Cu</sub> to incorporate more LiF, Li<sub>2</sub>S and organic SEI



 $\label{eq:Fig.6} \textbf{Fig. 6} | \textbf{Bridging the chemistry, formation and passivation of SEI}_{Cu}. The concurrent steps of SEI chemistry (FSI^ breakdown) first form the basic SEI ingredients during continuous ET (left), which then undergo an interfacial dissolution–precipitation equilibrium to be incorporated into the compact SEI_{Cu}$ 

layer (middle). The efficacy of  ${\rm SEI}_{\rm Cu}$  passivation strongly depends on the chemical identity of the organic solvent dictating the abundance of key passivating ingredients such as LiF, whereas an electrolyte-blocking SEI is desirable for limiting the necessary SEI reactions to effectively passivate Cu (right).

species relative to LiOH/Li<sub>2</sub>O, with a slightly increased F/C ratio. The SEI<sub>CII</sub> formed by CA at 0 V<sub>II</sub> exhibits compositional ratios similar to that formed by CP-Cu. As a more negative  $E_{\text{Cu}}$  imposes a larger driving force of electrolyte decomposition, these data suggest that the incorporation of more anion-derived species (LiF and Li<sub>2</sub>S) in the SEI<sub>CU</sub> layer can enhance the passivation of the Cu surface. Consequently, the  $SEI_{Cu}$  formed at 0  $V_{Li}$  leads to an almost doubled overpotential of Li<sup>0</sup>-nucleation compared to that formed at +1 V<sub>Li</sub> (Supplementary Fig. 15) $^{45-47}$ . Surface imaging of  $SEI_{Cu}$  by scanning electron microscopy (SEM) and atomic force microscopy (AFM) consistently shows a densely packed nanoparticulate morphology for the CA<sub>0V</sub>-Cu sample (Fig. 4j,k and Supplementary Figs. 16 and 17). Correspondingly, cryogenic electron microscopy (cryo-EM) reveals the formation of a monolithic passivating  $SEI_{Cu}$  layer on a Cu grid with a thickness of  $13.2 \pm 1.1$  nm, formed by CA at 0  $V_{1i}$  (Fig. 41). The lattice fringe of  $Li_2CO_3$  (d = 0.287 nm) embedded in an amorphous matrix was identified on the outer part of the SEI<sub>Cu</sub>.

#### Solvent-dependent interfacial reactivity and passivation

After understanding both the  $SEI_{Cu}$  reaction and formation, we further compared the initial galvanostatic E-t curves (i=-0.2 mA) of Li|Cu cells across different LiFSI-based liquid electrolytes, especially those previously demonstrating a high CE in LMAs (Fig. 5a)<sup>5,6,18</sup>. Interestingly, we discovered a consistent trend where  $E_{Cu}$  tends to drop much faster to 0  $V_{Li}$  in high-performance electrolytes, suggesting fewer electrons are spent in the irreversible  $SEI_{Cu}$  formation to effectively passivate the Cu surface (Fig. 5b,c). Switching from the baseline DME/1 M LiFSI electrolyte to other fluorinated electrolytes (2,2,3,3-tetrafluoro-1,4-dime thoxybutane, FDMB; 1,2-bis(2,2-difluoroethoxy)ethane, F4DEE; 2-(2-(2,2-difluoroethoxy)ethoxy)-1,1,1-trifluoroethane, F5DEE) with high CEs (-99.5% measured by the Aurbach method) resulted in dramatic decreases in the average passivation time ( $t_{OV}$ ), from >360 s to <150 s. High-concentration electrolytes (4 M LiFSI in DME and DEE) also exhibited much reduced  $t_{OV}$ .

A comparison of the first-CV behaviours of the same Cu micro-electrode reveals reduced current densities in the  $E_{\rm Cu}$  regions of direct ET (>+1 V<sub>Li</sub>) and Li UPD/UPS (<+0.5 V<sub>Li</sub>) for high-CE electrolytes (Fig. 5d,e and Supplementary Fig. 18). We quantified the differences in current densities ( $\Delta J$ ) between the first and fifth CVs at +1 and +0.5 V<sub>Li</sub> to qualitatively compare the relative contributions of direct ET and Li UPD processes towards SEI<sub>Cu</sub> formation, respectively. As seen in Fig. 5e,

the baseline DME/1 M LiFSI electrolyte exhibits much larger Δ/ at both potentials. All the other four high-CE electrolytes showed larger  $\Delta I$  at  $+1\,V_{Li}$  than at  $+0.5\,V_{Li}$ , suggesting higher contributions of the initial  $SEI_{Cu}$ passivation via direct ET. However, the comparably high  $\Delta$ / at both E values for the DME/1 M LiFSI electrolyte implies an ineffectiveness of the first step of direct ET towards Cu passivation, thus necessitating the  $second\,step\,of\,Li\,UPD\,to\,form\,more\,ing redients\,for\,SEI_{Cu}.\,Moreover, the$ even smaller  $\Delta J$  at +0.5  $V_{Li}$  of the fluorinated electrolytes (FxDEE) than the high-concentration electrolytes (DME/DEE) demonstrates their abilities to passivate Cu electrodes more effectively via the initial ET step. As the J values at +1 V<sub>Li</sub> remained unchanged after the second CV cycle, the similar |/| values across five different electrolytes are generally assigned to their comparable capacitive behaviours of EDL at the Cu surface (Supplementary Fig. 18). Furthermore, a comparison of the Li UPD peaks at  $+0.5 \, V_{Li}$  in the fifth CV cycle reveals a decreasing trend for electrolytes with higher CEs (Supplementary Fig. 18), suggesting higher electrolyte resistance of the resulting SEI<sub>cu</sub>.

Using F4DEE/1 MLiFSI electrolyte as an example, the non-washing XPS protocol was again applied to reveal similar decomposition products from FSI $^-$  breakdown, including LiF, Li $_2$ S, SO $_x$ , N–SO $_x$  and Li $_3$ N, among others (Supplementary Fig. 19). These results directly reveal that complete LiFSI decomposition can also occur at the Li-metal potential, even for a high-CE electrolyte.

To identify effective compositional descriptors accounting for more passivating SEI<sub>Cu</sub>, we further compared various atomic ratios of SEI<sub>CII</sub> of washed CP-Cu samples formed in different electrolytes (Fig. 5f-i and Supplementary Fig. 20). First, the O/F ratio consistently decreased from ~7 for the DME/1 M LiFSI electrolyte to ~2 for other high-concentration and fluorinated electrolytes, signalling increased LiF content (Fig. 5f). The ratios between the LiOH/Li<sub>2</sub>O and organic contents are similar for all electrolytes, except that the high-concentration DME/4 M LiFSI electrolyte exhibits slightly more organic content (Fig. 5g). Furthermore, the F/C ratios increased from the baseline DME/1 M LiFSI electrolyte (~0.5) to the high-CE electrolytes (~1.5), again confirming that more LiF was incorporated into the  $SEI_{Cu}$  than in the organic SEI (Fig. 5h). Correspondingly, the increased S/C ratios with increasing CE values show consistent increases of anion-derived species during SEI<sub>Cu</sub> formation (Fig. 5i). It should be noted that all samples were washed by DME following the same protocol. The enriched LiF and Li<sub>2</sub>S in SEI<sub>Cu</sub> should be mechanically robust enough to survive any possible dissolution or delamination during DME washing<sup>8,9</sup>.

Together, these data show that high-CE electrolytes exhibit lower electrochemical reactivity towards  ${\sf SEI}_{\sf Cu}$  formation, but their  ${\sf SEI}_{\sf Cu}$  contained more anion-derived species (LiF and Li\_2S) beneficial for passivating the Cu surface. The efficacy of  ${\sf SEI}_{\sf Cu}$  in passivating the Cu surface against continuous electrolyte decomposition does not depend on the amount of SEI ingredients formed electrochemically, but instead on how much of these ingredients can be effectively incorporated into the  ${\sf SEI}_{\sf Cu}$ . Such an apparently counterintuitive correlation between the magnitude of the interfacial reactivity and the efficacy of  ${\sf SEI}_{\sf Cu}$  passivation indicates that high-CE electrolytes can form sufficiently passivating  ${\sf SEI}_{\sf Cu}$  with minimized irreversible electrolyte decomposition.

# **Conclusions**

Overall, we have combined electrochemical analyses with XPS measurements to comprehensively elucidate SEI formation in LiFSI-based liquid electrolytes, using Cu electrode as a reaction platform. We have designed a method of combining washing and non-washing XPS analysis to elucidate the knowledge gaps between molecular- and material-level processes (Fig. 6). First, when  $E_{Cu}$  approaches 0  $V_{Li}$  under cathodic conditions, the S atoms of FSI<sup>-</sup> are prone to electrochemical reduction, causing anion breakdown via three basic steps: (1) S-F cleavage to form LiF and SO<sub>x</sub>, (2) S=O cleavage to form Li<sub>2</sub>S and Li<sub>2</sub>O and (3) stepwise N-S cleavage to form the N-SO<sub>x</sub> intermediate and Li<sub>3</sub>N. Meanwhile, electrochemical decomposition of organic solvent produces organic SEI species. Such SEI-forming reactions exhibit an *E*-dependence where initial and further  $SEI_{CII}$  formation occur at a high  $E_{CII}$  of >+1  $V_{II}$  via direct ET and at a low  $E_{Cu}$  of <+0.5  $V_{Li}$  via Li UPD, respectively<sup>48</sup>. Despite the active generation of various SEI ingredients from electrolyte decomposition, only a portion of the decomposition products precipitate at the Cu surface to form a monolithic  $SEI_{Cu}$  layer, while others can dissolve from the interface into the liquid layer. Consequently, an equilibrium is expected at the Cu/electrolyte interface between this dissolution and precipitation of the various SEI ingredients (Supplementary Note 2). Based on their relative abundance, a solubility trend is derived as  $\text{Li}_3\text{N/N-SO}_x\text{/-SO}_2\text{F} > \text{SO}_x > \text{Li}_2\text{S} > \text{LiF} > \text{Li}_2\text{O}/\text{LiOH}$ . The  $\text{SEI}_{\text{CII}}$  formed in the baseline DME/1 M LiFSI electrolyte was exclusively dominated by the LiOH/Li<sub>2</sub>O and organic species, whereas other high-CE electrolytes contained more anion-derived species (LiF and Li<sub>2</sub>S)<sup>36</sup>. The beneficial roles of these FSI<sup>-</sup>-derived species in passivating the Cu surface are evident from their increased content in SEI<sub>Cu</sub> formed at more negative E values. By contrast, the SEI<sub>Cu</sub> layers formed in other high-CE electrolytes incorporated much more anion-derive species, which simultaneously leads to faster passivation and reduced reactivity of the Cu/electrolyte interface. Therefore, such a solvent dependence of SEI<sub>CII</sub> passivation efficacy shows that the key to faster surface passivation lies in incorporating more passivating ingredients immediately following their generation, to effectively enable an 'electrolyteblocking' SEI<sub>Cu</sub> layer.

# Online content

Any methods, additional references, Nature Portfolio reporting summaries, source data, extended data, supplementary information, acknowledgements, peer review information; details of author contributions and competing interests; and statements of data and code availability are available at https://doi.org/10.1038/s41557-024-01689-5.

#### References

- Liu, J. et al. Pathways for practical high-energy long-cycling lithium metal batteries. Nat. Energy 4, 180–186 (2019).
- Yu, Z., Cui, Y. & Bao, Z. Design principles of artificial solid electrolyte interphases for lithium-metal anodes. *Cell Rep. Phys.* Sci. 1, 100119 (2020).
- Wang, H. et al. Liquid electrolyte: the nexus of practical lithium metal batteries. *Joule* 6, 588–616 (2022).

- Hobold, G. M. et al. Moving beyond 99.9% coulombic efficiency for lithium anodes in liquid electrolytes. *Nat. Energy* 6, 951–960 (2021).
- Yu, Z. et al. Molecular design for electrolyte solvents enabling energy-dense and long-cycling lithium metal batteries. *Nat. Energy* 5, 526–533 (2020).
- Yu, Z. et al. Rational solvent molecule tuning for high-performance lithium metal battery electrolytes. *Nat. Energy* 7, 94–106 (2022).
- Wang, H. et al. Efficient lithium metal cycling over a wide range of pressures from an anion-derived solid–electrolyte interphase framework. ACS Energy Lett. 6, 816–825 (2021).
- Cao, X. et al. Monolithic solid–electrolyte interphases formed in fluorinated orthoformate-based electrolytes minimize Li depletion and pulverization. *Nat. Energy* 4, 796–805 (2019).
- Kim, S. C. et al. Potentiometric measurement to probe solvation energy and its correlation to lithium battery cyclability. *J. Am. Chem.* Soc. 143, 10301–10308 (2021).
- 10. Zhang, Z. et al. Capturing the swelling of solid-electrolyte interphase in lithium metal batteries. Science **375**, 66–70 (2022).
- Niu, C. et al. Balancing interfacial reactions to achieve long cycle life in high-energy lithium metal batteries. *Nat. Energy* 6, 723–732 (2021).
- 12. Xiao, J. et al. Understanding and applying coulombic efficiency in lithium metal batteries. *Nat. Energy* **5**, 561–568 (2020).
- Adams, B. D., Zheng, J., Ren, X., Xu, W. & Zhang, J. Accurate determination of coulombic efficiency for lithium metal anodes and lithium metal batteries. Adv. Energy Mater. 8, 1702097 (2018).
- 14. Jin, Y. et al. Low-solvation electrolytes for high-voltage sodium-ion batteries. *Nat. Energy* **7**, 718–725 (2022).
- Sayavong, P. et al. Dissolution of the solid electrolyte interphase and its effects on lithium metal anode cyclability. J. Am. Chem. Soc. 145, 12342–12350 (2023).
- Xu, Y. et al. Promoting mechanistic understanding of lithium deposition and solid–electrolyte interphase (SEI) formation using advanced characterization and simulation methods: recent progress, limitations and future perspectives. Adv. Energy Mater. 12, 2200398 (2022).
- Yu, W., Yu, Z., Cui, Y. & Bao, Z. Degradation and speciation of Li salts during XPS analysis for battery research. ACS Energy Lett. 7, 3270–3275 (2022).
- Chen, Y. et al. Steric effect tuned ion solvation enabling stable cycling of high-voltage lithium metal battery. J. Am. Chem. Soc. 143, 18703–18713 (2021).
- Boyle, D. T. et al. Transient voltammetry with ultramicroelectrodes reveals the electron transfer kinetics of lithium metal anodes. ACS Energy Lett. 5, 701–709 (2020).
- Aurbach, D., Daroux, M., Faguy, P. & Yeager, E. The electrochemistry of noble metal electrodes in aprotic organic solvents containing lithium salts. J. Electroanal. Chem. Interfacial Electrochem. 297, 225–244 (1991).
- Gu, Y. et al. Lithiophilic faceted Cu(100) surfaces: high utilization of host surface and cavities for lithium metal anodes. *Angew. Chem. Int. Ed.* 58, 3092–3096 (2019).
- 22. He, J. et al. Structures of solid-electrolyte interphases and impacts on initial-stage lithium deposition in pyrrolidinium-based ionic liquids. *ChemElectroChem* **8**, 62–69 (2021).
- Débart, A., Dupont, L., Poizot, P., Leriche, J.-B. & Tarascon, J. M. A transmission electron microscopy study of the reactivity mechanism of tailor-made CuO particles toward lithium. J. Electrochem. Soc. 148, A1266 (2001).
- Huang, W. et al. Nanostructural and electrochemical evolution of the solid-electrolyte interphase on CuO nanowires revealed by cryogenic-electron microscopy and impedance spectroscopy. ACS Nano 13, 737–744 (2019).

- Xu, K. Interfaces and interphases in batteries. J. Power Sources 559, 232652 (2023).
- 26. Xu, K. Electrolytes, Interfaces and Interphases: Fundamentals and Applications in Batteries (Royal Society of Chemistry, 2023).
- 27. Moshkovich, M., Gofer, Y. & Aurbach, D. Investigation of the electrochemical windows of aprotic alkali metal (Li, Na, K) salt solutions. *J. Electrochem.* Soc. **148**, E155 (2001).
- 28. Aurbach, D. et al. Design of electrolyte solutions for Li and Li-ion batteries: a review. *Electrochim. Acta* **50**, 247–254 (2004).
- Schiffer, Z. J., Chung, M., Steinberg, K. & Manthiram, K. Selective electrochemical reductive amination of benzaldehyde at heterogeneous metal surfaces. *Chem. Catal.* 3, 100500 (2023).
- 30. Menkin, S. et al. Toward an understanding of SEI formation and lithium plating on copper in anode-free batteries. *J. Phys. Chem. C* **125**, 16719–16732 (2021).
- Tan, S. et al. Unravelling the convoluted and dynamic interphasial mechanisms on Li metal anodes. Nat. Nanotechnol. 18, 243–249 (2023).
- 32. Sasaki, T., Williams, R. S., Wong, J. S. & Shirley, D. A. Radiation damage studies by X-ray photoelectron spectroscopy. I. Electron irradiated LiNO<sub>3</sub> and Li<sub>2</sub>SO<sub>4</sub>. *J. Chem. Phys.* **68**, 2718–2724 (1978).
- Agostini, M., Xiong, S., Matic, A. & Hassoun, J. Polysulfide-containing glyme-based electrolytes for lithium sulfur battery. Chem. Mater. 27, 4604–4611 (2015).
- Wood, K. N. & Teeter, G. XPS on Li-battery-related compounds: analysis of inorganic SEI phases and a methodology for charge correction. ACS Appl. Energy Mater. 1, 4493–4504 (2018).
- Kerner, M., Plylahan, N., Scheers, J. & Johansson, P. Thermal stability and decomposition of lithium bis(fluorosulfonyl)imide (LiFSI) salts. RSC Adv. 6, 23327–23334 (2016).
- Huang, W., Wang, H., Boyle, D. T., Li, Y. & Cui, Y. Resolving nanoscopic and mesoscopic heterogeneity of fluorinated species in battery solid-electrolyte interphases by cryogenic electron microscopy. ACS Energy Lett. 5, 1128–1135 (2020).
- Shadike, Z. et al. Identification of LiH and nanocrystalline LiF in the solid–electrolyte interphase of lithium metal anodes. *Nat. Nanotechnol.* 16, 549–554 (2021).
- Zachman, M. J., Tu, Z., Choudhury, S., Archer, L. A. & Kourkoutis, L. F. Cryo-STEM mapping of solid-liquid interfaces and dendrites in lithium-metal batteries. *Nature* 560, 345–349 (2018).
- Dhattarwal, H. S., Chen, Y.-W., Kuo, J.-L. & Kashyap, H. K. Mechanistic insight on the formation of a Solid Electrolyte Interphase (SEI) by an acetonitrile-based superconcentrated [Li][TFSI] electrolyte near lithium metal. J. Phys. Chem. C 124, 27495–27502 (2020).

- Han, J., Zheng, Y., Guo, N. & Balbuena, P. B. Calculated reduction potentials of electrolyte species in lithium-sulfur batteries. *J. Phys. Chem. C* 124, 20654–20670 (2020).
- Aurbach, D., Daroux, M. L., Faguy, P. W. & Yeager, E. Identification of surface films formed on lithium in dimethoxyethane and tetrahydrofuran solutions. *J. Electrochem. Soc.* 135, 1863–1871 (1988).
- 42. Aurbach, D., Daroux, M., McDougall, G. & Yeager, E. B. Spectroscopic studies of lithium in an ultrahigh vacuum system. *J. Electroanal. Chem.* **358**, 63–76 (1993).
- 43. Zhao, Z., Huang, J. & Peng, Z. Achilles' heel of lithium-air batteries: lithium carbonate. *Angew. Chem. Int. Ed.* **57**, 3874–3886 (2018).
- 44. Qian, J. et al. Initial steps in forming the electrode-electrolyte interface: H<sub>2</sub>O adsorption and complex formation on the Ag(111) surface from combining quantum mechanics calculations and ambient pressure X-ray photoelectron spectroscopy. J. Am. Chem. Soc. 141, 6946–6954 (2019).
- Xu, Y. et al. Sweeping potential regulated structural and chemical evolution of solid-electrolyte interphase on Cu and Li as revealed by Cryo-TEM. Nano Energy 76, 105040 (2020).
- Oyakhire, S. T. et al. Correlating the formation protocols of solid electrolyte interphases with practical performance metrics in lithium metal batteries. ACS Energy Lett. 8, 869–877 (2023).
- Lu, P., Li, C., Schneider, E. W. & Harris, S. J. Chemistry, impedance and morphology evolution in solid electrolyte interphase films during formation in lithium ion batteries. *J. Phys. Chem. C* 118, 896–903 (2014).
- 48. Sun, S. et al. The crucial role of electrode potential of a working anode in dictating the structural evolution of solid electrolyte interphase. *Angew. Chem. Int. Ed.* **61**, e202208743 (2022).

**Publisher's note** Springer Nature remains neutral with regard to jurisdictional claims in published maps and institutional affiliations.

Springer Nature or its licensor (e.g. a society or other partner) holds exclusive rights to this article under a publishing agreement with the author(s) or other rightsholder(s); author self-archiving of the accepted manuscript version of this article is solely governed by the terms of such publishing agreement and applicable law.

© The Author(s), under exclusive licence to Springer Nature Limited 2024

<sup>1</sup>Department of Chemical Engineering, Stanford University, Stanford, CA, USA. <sup>2</sup>Department of Chemistry, Stanford University, Stanford, CA, USA. <sup>3</sup>Department of Materials Science and Engineering, Stanford University, Stanford, CA, USA. <sup>4</sup>SUNCAT Center for Interface Science and Catalysis, SLAC National Accelerator Laboratory, Menlo Park, CA, USA. <sup>5</sup>Department of Mechanical Engineering, University of Wisconsin–Madison, Madison, WI, USA. <sup>6</sup>Energy Storage and Distributed Resources Division, Lawrence Berkeley National Laboratory, Berkeley, CA, USA. <sup>7</sup>Computational Chemistry Lab, Department of Chemical Engineering, National Taiwan University of Science and Technology, Taipei, Taiwan. <sup>8</sup>Department of Energy Science and Engineering, Stanford University, Stanford, CA, USA. <sup>9</sup>Stanford Institute for Materials and Energy Sciences, SLAC National Accelerator Laboratory, Menlo Park, CA, USA. —e-mail: yicui@stanford.edu; zbao@stanford.edu

# Methods

#### **Material preparation**

Celgard 2325 (25-µm-thick, polypropylene/polyethylene/polypropylene) was purchased from Celgard. Cu foil (25-µm-thick) was purchased from Alfa Aesar. Thick Li foil (750-µm-thick) was purchased from MSE Supplies. All other components for 2032-type coin cells were purchased from MTI. LiFSI was purchased from Arkema. High-purity DME (anhydrous, 99.5%) was purchased from Sigma and used directly. DEE (99%, ACROS) was purchased from Fisher Scientific and purified for further use<sup>18</sup>. Fluorinated solvents such as F-DEE and FDMB were synthesized, purified and dried following the procedures described previously<sup>5,6</sup>. Fresh Li foil was added into all solvents inside the glovebox to further remove trace water.

#### Coin-cell fabrication

All coin cells were fabricated as 2032-type using Celgard 2325 as the separator in an Ar-filled glovebox. In a typical procedure (for example, for a Li|Cu half cell), a spring was placed in a negative coin-cell case, followed by a stainless-steel spacer and a thick Li foil (750- $\mu$ m-thick) with a diameter of 7/16 inch, then 20  $\mu$ l of electrolyte was added to the surface of the Li foil and one piece of Celgard 2325 separator placed on top of the foil. This was followed by the addition of another 20  $\mu$ l of electrolyte. Finally, a Cu foil, another stainless-steel spacer and the stainless-steel positive case were placed sequentially. The coin cell was finally subjected to a crimper press.

#### **Electrochemical measurements**

Both chronoamperometry (CA) and CP were performed on a Biologic MPG-2 potentiostat. All coin cells were rested at open circuit for 3 h before testing. The typical galvanostatic (CP) cycling experiment used in this study involved applying a constant I = -0.2 mA and cycling between 0 and 1  $V_{Li}$  100 times, and the E-t profiles of the first cycles were used to compare the efficacy of  $SEl_{Cu}$  passivation. The typical CA experiments involved first lowering the  $E_{Cu}$  to the target potential by applying a constant I = -0.2 mA, followed by holding at the cutoff E for at least 3 h. Three-electrode CV was performed in a beaker cell with -2 ml of liquid electrolyte, using a freshly polished Cu micro-electrode as the working electrode, and Li-metal foils as the reference and counter electrodes.

# Coin-cell disassembly and sample washing/transfer

The Cu samples were first carefully retrieved from the tested Li|Cu cells after they were subjected to a disassembling press, where a thin layer of liquid was typically observed to conformally cover the Cu surface. For non-washing XPS, the liquid-covered samples were directly mounted on the XPS sample stage and transferred to the instrument in an air-free fashion. For XPS with solvent washing, 20  $\mu$ l of pristine DME was dropped by pipette at the centre of the Cu sample, and naturally spread out to cover the entire surface. A piece of clean Kimwipe was then used to gently touch the Cu sample to remove liquid from the surface using capillary force. This process was repeated at least twice. XPS data consistently confirmed effective removal of residual liquid (absence of a LiFSI salt peak in F1s spectra) The washed samples were typically pumped in the XPS intro chamber for >2 h, allowing the samples to be sufficiently dried and thus ensuring high-quality XPS datasets.

#### XPS

All XPS data were collected with a PHI VersaProbe 3 XPS with an Al K $\alpha$  source. The X-ray settings were 200  $\mu$ m, 50 W and 15 kV. During XPS measurements, the time step was 50 ms and pass energy 112 eV. Both electron and ion neutralization sources were used. All depth profiling was achieved using the same Ar $^+$  sputtering condition (1 kV, 0.7  $\mu$ A, 2 × 2 mm) with a calibrated etching rate of -3 nm min $^{-1}$  using SiO $_2$  (ref. 17). We found that a 3-min Ar $^+$  sputtering of SEI $_{\text{Cu}}$  for the CP-Cu samples under this setting typically started to expose the underlying Cu substrate, leading to an estimated thickness of -10 nm (ref. 47).

High-resolution XPS spectra were deconvoluted in CasaXPS 2.3.23 software. All XPS spectra were first calibrated by referring to the LiF peak at BE = 684.8 eV or the adventitious carbon peak at BE = 284.8 eV. Additional calibration may be necessary for specific elements to compensate for excessive charging, using other low-BE references including Li<sub>2</sub>O (528.2 eV for O 1s), Li<sub>2</sub>S (160.2 eV for S 2p) and Li<sub>3</sub>N (396.2 eV for N 1s). During peak fitting of most elements, the FWHM values of all peaks were typically constrained between 1.5 and 1.8 eV to obtain reasonable fitting results. For S 2p spectra, the BE differences between the two peaks of the same doublet were typically constrained to 1.0–1.2 eV. The relative atomic percentages were quantified using MultiPak software after accounting for the elemental sensitivity factors of the XPS instrument. Statistical analysis of the XPS fitting results in this work is presented in Supplementary Table 1.

#### **Material characterizations**

The Raman spectra of the electrolytes solutions were obtained on a Horiba XploRA+ confocal Raman set-up with a 532-nm excitation laser. After the electrochemical test, the retrieved Cu sample from the disassembled Li|Cu cell was sealed in a narrow (0.1-cm width) quartz cuvette in an Ar-filled glovebox before Raman measurements. SEM images were collected using an FEI Magellan 400 XHR scanning electron microscope. AFM measurements were collected using a Bruker Icon Dimension instrument with a SCANASYST-AIR probe (Bruker AFM Probes; nominal spring constant of 0.4 N m<sup>-1</sup>, resonance frequency of 70 kHz and tip radius of 2 nm). The scan resolution was set to 256 × 256 pixels with a scan rate of 0.4 Hz. A Thermo Fisher Titan 80-300 environmental transmission electron microscope at an accelerating voltage of 300 kV and a Gatan 626 side-entry holder were used for cryo-transmission electron microscopy (TEM) experiments. Cryo-TEM sample preparations prevent air and moisture exposure and reduce electron beam damage, as described previously<sup>49</sup>. The TEM was equipped with an aberration corrector in the image-forming lens, which was tuned before imaging. Cryo-TEM images were acquired by a Oneview camera. Cryo-TEM images were taken with an electron dose rate of ~300  $e^-$  Å<sup>-2</sup> s<sup>-1</sup> with an exposure time of 0.3 s for each image.

# **DFT calculations**

Electronic calculations were performed with the Quantum ESPRESSO code<sup>50</sup>, in which energetics are obtained in a self-consistent fashion, with periodic plane-waves and ultrasoft pseudopotentials. The BEEFvdW exchange-correlation functional was used to provide a reasonable description of van der Waals forces while maintaining an accurate prediction of chemisorption energies<sup>51</sup>. The plane-wave and density cutoffs were 500 and 5,000 eV, respectively, with a Fermi-level smearing width of 0.1 eV. Optimized structures were realized when Hellmann-Feynman forces were below 0.05 eV Å<sup>-1</sup>. The adsorption energies on a Li(100) surface were evaluated using five-layer  $(4 \times 4)$  supercells with the bottom two layers constrained and a vacuum layer of 17.4 Å, and  $[4 \times 4 \times 1]$  Monkhorst-Pack k-point grids were used. Similarly, the adsorption energies determined on Cu(100) surface were evaluated using four-layer (3 × 4) supercells with the bottom two layers constrained and a vacuum layer of 12 Å with the same k-point grid setting. FSI is an anion in solution, and it is difficult to ascertain the energetics of the species. We thus assume that the gaseous species trend similarly in reactivity, such that the adsorbed state as referenced to the gas species will correlate with the ionized counterpart due to similar positive core arrangement and resulting charge densities from DFT. All computational data will be released as part of the Catalysis-hub.org repository<sup>52</sup>.

# **AIMD simulations**

All AIMD simulations in this study were performed using the Vienna Ab initio Simulation Package (VASP) with the projector-augmented wave (PAW) method proposed by Perdew–Burke–Ernzerhof (PBE) for the exchange–correlation energy functional 53–55. The vdW D3 correction

proposed by Grimme was considered to include the vdW correction<sup>56</sup>. The energy cutoff for the plane-wave basis expansion was employed to be 400 eV, and the Monkhorst-Pack scheme was used for k-point sampling and Brillouin zone integration. The Li and Cu bulk was optimized first, then the Li(100) and Cu(100) crystallographic planes were cleaved from the optimized bulk structure as previous XRD calculation results indicated that the Li(100) and Cu(100) facets are the preferred orientations. Here we constructed four layers of Cu(100) surface in a  $p(4 \times 4)$ supercell as a Cu current collector model, in which the bottom layer was replaced with He atoms to prevent interactions between neighbouring slabs. We then constructed a pristine Li surface by incorporating three Li(100) layers onto the Cu(100) surface, as shown in Supplementary Fig. 10. The electrolyte cell was composed of 1 M LiFSI in a DME solvent, and the numbers of solvent and ion pairs in the simulation cell were chosen corresponding to densities of 0.86 g cm<sup>-3</sup> for DME. Within a canonical ensemble (NVT) maintained at 400 K, the AIMD simulations underwent equilibration, extending over a duration of 15 ps and utilizing a time step of 1 fs. Bader charge analysis was used to estimate the charge transfer between the electrolyte and the anode surface.

# **Data availability**

All data supporting the findings of this study are included in the Article and its Supplementary Information. Source data are provided with this paper.

#### References

- Li, Y. et al. Atomic structure of sensitive battery materials and interfaces revealed by cryo-electron microscopy. Science 358, 506–510 (2017).
- Giannozzi, P. et al. Quantum ESPRESSO: a modular and open-source software project for quantum simulations of materials. J. Phys. Condens. Matter 21, 395502 (2009).
- 51. Wellendorff, J. et al. Density functionals for surface science: exchange-correlation model development with Bayesian error estimation. *Phys. Rev. B* **85**, 235149 (2012).
- 52. Winther, K. T. et al. Catalysis-Hub.Org, an open electronic structure database for surface reactions. Sci. Data **6**, 75 (2019).
- Kresse, G. & Furthmüller, J. Efficiency of ab-initio total energy calculations for metals and semiconductors using a plane-wave basis set. Comput. Mater. Sci. 6, 15–50 (1996).
- Kresse, G. & Hafner, J. Ab initio molecular dynamics for liquid metals. Phys. Rev. B 47, 558–561 (1993).
- Blöchl, P. E. Projector augmented-wave method. *Phys. Rev. B* 50, 17953–17979 (1994).
- Grimme, S., Antony, J., Ehrlich, S. & Krieg, H. A consistent and accurate ab initio parametrization of density functional dispersion correction (DFT-D) for the 94 elements H-Pu. J. Chem. Phys. 132, 154104 (2010).

# Acknowledgements

This work is supported by the US Department of Energy, under the Assistant Secretary for Energy Efficiency and Renewable Energy, Office of Vehicle Technologies, the Battery Materials Research Program and Battery500 Consortium. Y. Cui (0000-0002-6103-6352) acknowledges cryo-EM support from the US Department of Energy. Office of Basic Energy Sciences, Division of Materials Science and Engineering under contract no. DE-ACO2-76SF00515. Part of this work was performed at the Stanford Nano Shared Facilities, supported by the National Science Foundation under award no. ECCS-2026822. This research was also in part supported by the US Department of Energy Office of Science, Office of Basic Energy Sciences, Chemical Sciences, Geosciences and Biosciences Division Catalysis Science Program to the SUNCAT Center for Interface Science and Catalysis. M.T.T. acknowledges computer time allocation for SUNCAT-FWP (m2997) at the National Energy Research Scientific Computing Center, a DOE Office of Science User Facility supported by the Office of Science of the US Department of Energy under contract no. DE-ACO2-05CH11231. K.-Y.L. acknowledges support from the Taiwan Science and Technology Hub at Stanford University. S.J.H. was supported by the Laboratory Directed Research and Development Program of Lawrence Berkeley National Laboratory under US Department of Energy contract no. DE-ACO2-05CH11231. J. Jamtgaard is thanked for assistance with XPS experiments. J. Holoubek and J. Florian are thanked for commenting on a draft of this manuscript.

# **Author contributions**

W.Y., Y. Cui (0000-0002-6103-6352) and Z.B. conceived the idea. Y. Cui (0000-0002-6103-6352) and Z.B. directed the project. W.Y. designed the logic flow and performed all XPS experiments and analyses. W.Y. and D.T.B. performed electrochemical measurements. K.-Y.L. performed molecular dynamics simulations. M.T.T. performed DFT calculations. Y. Cui (0000-0001-8219-1856) and G.F. performed cryo-EM measurements. Z.H. performed Raman measurements. R.X. and L.M. performed AFM measurements. Z.Y. synthesized fluorinated solvents. Y. Chen and Y.L. helped with electrolyte preparation and coin-cell fabrication, W.L. performed computational simulations of SEI formation. All authors contributed to the interpretation of the results. W.Y., Y. Cui (0000-0002-6103-6352) and Z.B. co-wrote and revised the manuscript.

#### **Competing interests**

The authors declare no competing interests.

# **Additional information**

**Supplementary information** The online version contains supplementary material available at https://doi.org/10.1038/s41557-024-01689-5.

**Correspondence and requests for materials** should be addressed to Yi Cui or Zhenan Bao.

**Peer review information** *Nature Chemistry* thanks Jijian Xu and the other, anonymous, reviewer(s) for their contribution to the peer review of this work.

**Reprints and permissions information** is available at www.nature.com/reprints.